Structured near-infrared magnetic circular dichroism spectra of the Mn4CaO5 cluster of PS II in T. vulcanus are dominated by Mn(IV) d-d 'spin-flip' transitions

Jennifer Morton, Maria Chrysina, Vincent S.J. Craig, Fusamichi Akita, Yoshiki Nakajima, Wolfgang Lubitz, Nicholas Cox, Jian-Ren Shen, Elmars Krausz

PII: S0005-2728(17)30156-1
DOI: doi:10.1016/j.bbabio.2017.10.004
Reference: BBABIO 47843

To appear in:

Received date: 21 April 2017
Revised date: 17 October 2017
Accepted date: 19 October 2017

Please cite this article as: Jennifer Morton, Maria Chrysina, Vincent S.J. Craig, Fusamichi Akita, Yoshiki Nakajima, Wolfgang Lubitz, Nicholas Cox, Jian-Ren Shen, Elmars Krausz , Structured near-infrared magnetic circular dichroism spectra of the Mn4CaO5 cluster of PS II in T. vulcanus are dominated by Mn(IV) d-d 'spin-flip' transitions. The address for the corresponding author was captured as affiliation for all authors. Please check if appropriate. Bbabio(2017), doi:10.1016/j.bbabio.2017.10.004

Structured Near-Infrared Magnetic Circular Dichroism spectra of the Mn_4CaO_5 cluster of PS II in *T. Vulcanus* are dominated by Mn(IV) d-d 'spin-flip' transitions

Jennifer Morton[1], Maria Chrysina[2], Vincent S.J. Craig[1], Fusamichi Akita[3,4], Yoshiki Nakajima[3], Wolfgang Lubitz[2], Nicholas Cox[1,2], Jian-Ren Shen[3]and Elmars Krausz[1]

[1]Research School of Chemistry, Australian National University, Canberra, Australia

[2]Max-Planck-Institut für Chemische Energiekonversion, Stiftstr. 34-36, 45470 Mülheim an der Ruhr, Germany

[3]Research Institute for Interdisciplinary Science, Graduate School of Natural Science and Technology, Department of Biology, Faculty of Science, Okayama University, Okayama, Japan

[4]Japan Science and Technology Agency, PRESTO, 4-1-8 Honcho, Kawaguchi, Saitama 332-0012, Japan

Email: elmars.krausz@anu.edu.au Fax:+61-2-6125-0750

Running Head: S-State MCD

Keywords: Photosystem II, S-states, Oxygen Evolving Center, Charge-Transfer, Magnetic Circular Dichroism.

Abbreviations:

Photosystem II; PSII
Near Infrared; near-IR
Ultra Violet/Visible; UV/Vis
Circular Dichroism; CD
Magnetic Circular Dichroism; MCD
Variable Temperature Variable Field; VTVH
Electron Paramagnetic Resonance; EPR
Oxygen Evolving Complex; OEC
Ligand-to-Metal Charge Transfer; LMCT
manganese catalase; MnCat
chlorophyll-a; Chl-a
tris(hydroxymethyl)aminomethane; Tris
continuous wave; CW
Supplementary Information; SI

ABSTRACT

Photosystem II passes through four metastable S-states in catalysing light-driven water oxidation. Variable temperature variable field (VTVH) Magnetic Circular Dichroism (MCD) spectra in PS II of *Thermosynochococcus (T.) vulcanus* for each S-state are reported. These spectra, along with assignments, provide a new window into the electronic and magnetic structure of Mn_4CaO_5. VTVH MCD spectra taken in the S_2 state provide a clear g = 2, $S = 1/2$ paramagnetic characteristic, which is entirely consistent with that known by EPR. The three features, seen as positive (+) at 749 nm, negative (-) at 773 nm and (+) at 808 nm are assigned as $^4A \rightarrow {}^2E$ spin-flips within the d^3 configuration of the Mn(IV) centres present. This assignment is supported by comparison(s) to spin-flips seen in a range of Mn(IV) materials. S_3 exhibits a more intense (-) MCD peak at 764 nm and has a stronger MCD saturation characteristic. This S_3 MCD saturation behaviour can be accurately modelled using parameters taken directly from analyses of EPR spectra. We see no evidence for Mn(III) d-d absorption in the near-IR of any S-state. We suggest that Mn(IV)-based absorption may be responsible for the well-known near-IR induced changes induced in S_2 EPR spectra of *T. vulcanus* and not Mn(III)-based, as has been commonly assumed. Through an analysis of the nephelauxetic effect, the excitation energy of S-state dependent spin-flips seen may help identify coordination characteristics and changes at each Mn(IV). A prospectus as to what more detailed S-state dependent MCD studies promise to achieve is outlined.

1 INTRODUCTION

The light driven chemical conversion of water to molecular oxygen and protons is performed in nature by a single enzyme, the Photosystem II (PSII) pigment-protein supercomplex[1-5]. Light absorption is followed by transfer of excitation to the reaction centre of PS II, leading to subsequent charge separation and the creation of a powerful Chl-a based oxidant, $P680^{\bullet+}$. This radical cation has the potential needed to oxidise water. Water oxidation is performed in a step-wise fashion through the coupling of $P680^{\bullet+}$ to the Mn_4CaO_5 cluster of the oxygen-evolving complex (OEC) via a redox active tyrosine residue (Tyr_Z). Each light absorption event, followed by charge separation, then proceeds to oxidise the cluster by extracting a single electron. After four oxidation events, the cluster then takes four electrons from two molecules of water, releasing molecular oxygen whilst returning the OEC to its least oxidised configuration[6]. The catalytic cycle of PS II is described in terms of a series of intermediate (S_i) states, where the subscript i denotes the number of stored oxidising equivalents in the manganese cluster.

Significant advances have recently been made in a broad range of experimental studies [7] focussing on the OEC and its Mn_4CaO_5 cluster in particular. The imperative has been to determine a detailed mechanism of water oxidation. Of greatest significance in this quest have been improvements in structural data [2], including the spectacular development of free electron laser-based femtosecond X-ray techniques[8] [9] [10]. Structures now exist for the resting state S_1 as well as S_3, which is the ultimate metastable state prior to O-O bond formation.

Crystallographic data alone cannot provide the level of detail needed to determine the electronic structure of the OEC and subsequently the mechanism of water oxidation. In this paper we describe the utility of Magnetic Circular Dichroism (MCD) as an incisive probe of the electronic structure of the Mn_4CaO_5 cluster, as poised in each metastable S-state. The MCD technique [11] is a natural partner to EPR spectroscopies [12, 13]. It has particular sensitivity towards open-shell metal systems. This characteristic allows the weakly absorbing features associated with d-d transitions of manganese ions within the Mn_4CaO_5 cluster to be distinguished from (the MCD of) far stronger chromophores present in PS II. The MCD technique also has the advantage of not being compromised by rapid magnetic relaxation processes. MCD displays equivalent sensitivity in both even and odd electron systems. Strong magnetic fields (>1 T) and low temperatures (<4 K) can create a situation where Zeeman splittings are comparable to both kT and ground state electronic energy spacings. MCD signals then become non-linear in magnetic field strength [14, 15]. Analysis of these curvatures is very sensitive to magnetic coupling between metal ions [16]. MCD thus promises to be a powerful and multi-faceted window on and into the Mn_4CaO_5 cluster.

It has long been known that near-IR illumination of PS II in the 700 nm - 900 nm region gives rise to dramatic changes in the EPR spectra of the Mn_4CaO_5 cluster. In particular, near-IR illumination of the S_2 state at 140 K has been shown to change the spin configuration of the S_2 ground state [17-19] There are two electronic configurations of S_2, a low spin (S = 1/2, multiline) state and a high spin (S = 5/2, $g \geq 4.1$) state. These have been assigned to two proposed structural forms of the Mn_4CaO_5 cluster[20, 21].

Near-IR illumination at lower temperatures (<20 K) can facilitate the formation of intermediates in

which an electron is taken from Tyr_Z and returned to the Mn_4CaO_5 cluster [22]. For the S_3 state, near-IR illumination at ≈10 K generates a distinctive EPR 'split signal', characteristic of an organic radical species coupled to a high-spin metal-based magnetic moment. This split signal for S_3 is ascribed to an $S_2Y_Z^{\bullet}$ -like intermediate [23] [24, 25] [26, 27]. The EPR action spectra of the S_2 and S_3 near-IR induced photo-conversion processes, as well overall yields, are similar. Both peak at ≈760 nm [28] and both processes are reversible upon warming.

The Mn_4CaO_5 based absorption responsible for the S_2 photo-activity has variously been attributed [17] [29] [30] to a d-d transition within the Mn(III) d^4 configuration(s) or a charge transfer (mixed valence) absorption(s) of neighbouring Mn(III)-Mn(IV) pair(s). By contrast, the photophysical activity in S_3 has also been addressed by proposing the presence of a spin-allowed, low energy d-d transition of a trigonal-bipyramidal Mn(IV) structure proposed [31]for the 'open' form of the S_3 state.

We recently reported [32] OEC based MCD features in PS II core complexes of *T. vulcanus* evident at 770 nm and 800 nm. These MCD features were strongly temperature dependent and saturated at high magnetic fields, indicating a predominantly paramagnetic species. The 770 nm-centered feature seen was provisionally assigned to a $d_z^2 \rightarrow d_{x2-y2}$ transition of a Mn(III) within the Mn_4CaO_5 cluster of the OEC, based on an analogy to a feature of similar amplitude seen in a manganese catalase (MnCat) [33-35], an enzyme that is structurally related to the OEC [36].

This study was able to clearly establish the chromophores responsible for stronger MCD features that overlap with weaker MCD signals associated with the OEC. The interfering signals at shorter wavelengths are primarily due to temperature-independent, B-term MCD arising from Chl-a based excitations. These originate from both a small (1%) component [37] of PS I present in the PS II preparation, as well as long-wavelength charge transfer absorption [38] of PS II. Strongly temperature dependent (C-term) MCD at longer wavelengths is due to Ligand-to-Metal Charge Transfer (LMCT) transitions of oxidised cyt b_{559} and cyt c_{550}. The MCD C-term characteristics of these LMCT transitions [39] make them difficult to separate from the (weaker) OEC based bands, as the latter have similar field and temperature dependencies.

In the initial report, our PS II core complexes were not poised in a specific S-state of the enzyme. After handling the sample in minimal light and a brief (5 minute) dark adaption period, the sample would have been predominantly in the (stable) S_1 state, with perhaps some S_2 and S_0 contributions. In response to the limitations of the exploratory study, we have made significant improvements in sample illumination protocols, sample cell design and overall spectrometer performance. These enhancements have led to a ≈10 fold increase in sensitivity as well as a ≈100 fold improvement in baseline stability.

In this paper, we report variable-temperature, variable-field (VTVH) MCD spectra for PS II which has been pre-flashed to create a well-defined S_1 state and advanced further to the S_2, S_3 and S_0 states in the usual way, i.e. via one or more closely spaced (≈3 Hz) and intense nanosecond YAG laser-flashes. We also report the four-flash spectrum, which restarts the Kok cycle. Apart from a pre-flashed and fully dark-adapted S_1 state, laser-flashed samples are invariably mixtures of S-states, owing to S-state advancement 'misses' and 'double hits'. We use the labels f0(S_1), f1(S_2), f2(S_3), f3(S_0) for *spectra* of the 0, 1, 2, 3 flash-

advanced samples, having S_1, S_2, S_3 and S_0 as targeted components. Appropriate calibration and manipulation of these spectra allow individual S-state spectra to be determined.

The phenomenology seen, that of a stepwise increase in the number of Mn_4CaO_5 features in MCD spectra in moving from S_1 to S_2, corresponding to an oxidation of a Mn(III) to a Mn (IV) at each step combined with the narrowness of spectral features observed, has led us to consider the possibility of an assignment of these features as arising from 'spin-flips' of the d^3 configuration of the Mn(IV) ions and *not* assignments based on transitions between Jahn-Teller split levels of tetragonally-distorted (six coordinate) d^4 Mn(III) configuration which, in all the examples in the literature, exhibit broader spectral features in absorption and MCD.

2 Materials and Methods

2.1 *Spectrometer System Improvements*

The basic spectrometer system utilised, capable of measuring absorption, CD and MCD spectra, has been previously described [40] [41]. A number of significant enhancements to the spectrometer system have been introduced. These improvements have led to a greatly increased sensitivity and stability of the system. In particular, the issue of zero levels and field dependent baseline in MCD has been fully resolved. The enhancements implemented and performance characteristics achieved are provided in the SI_2.1.

2.2 *Hydrophobic/Lipophobic Sample Cells*

The increased stability and sensitivity of our spectrometer has placed a far greater emphasis on limitations arising from the poor and variable (2-10%) transmission of samples at low temperatures. This low transmission was due to the characteristic opalescence of thick, low temperature glasses formed when using sample cell designs developed previously [42]. We were able to create highly reproducible samples with ten times greater transmission, by coating the sample cell with a thin but robust hydrophobic/lipophobic film. Samples frozen in these coated cells also exhibited far less strain birefringence, which enabled reproducible MCD baselines. A description of the development, production, and performance characteristics of these cells is provided in SI_2.2.

2.3 *Sample Illumination Systems and Protocols*

Samples were advanced into the higher S-states using the well-established 'saturating flash' technique of illumination by intense 5 ns flashes from a high power Q-switched YAG laser operating at 532 nm, in our case an injection-seeded Continuum Powerlite 8000. In our optical experiments, samples needed to be flashed with the sample cell already loaded with PS II sample and the cell installed in the sample rod. As the optical density of the sample at 532 nm was ≈4 OD units, the ≈300 mJ pulses from the laser were split into two equal intensity components, illuminating both the back and front of the sample cell simultaneously.

To poll a pre-loaded PS II sample accurately into a uniform S_1 state, the sample was pre-flashed once and left in the dark for 60 minutes before transfer to the cryostat. S_1 is the resting state of the OEC, However, a fraction of the S_1 population will have been formed by the slow decay of an S_0 component of the population, S_0 having been created when the sample was exposed to light. This S_0 decay process leaves

a corresponding fraction of the Tyr_D population reduced. A uniform S_1 population is created by the pre-flash protocol. Upon flashing, the S_1 population with Tyr_D reduced is activated to oxidise the Tyr_D and not the OEC. Any S_0 population present is advanced to S_1 and higher S_2 and S_3 populations created by the flash decay back to S_1 during the 60 minute dark adaptation period.

To poise the sample in higher S-states, so as to enable the measurement of f1(S_2), f2(S_3) and f3(S_3) spectra, the pre-flash procedure was repeated and the sample then flashed 1, 2 or 3 times, with pulses spaced by 0.3 s. The sample rod was then transferred to the superconducting magnet cryostat via a lock and frozen within ≈1-2 minutes. This process is rapid enough for thermophilic cyanobacterial samples, as they display[43]slow S-state deactivation rates. The rapid-action docking system was constructed so that the transfer to the cryostat could be performed with the sample kept in complete darkness, thus avoiding unintentional scrambling of S-states. The apparatus is described in SI_2.3.

For near-IR illuminations at 775 nm, a ≈300 mW continuous wave (CW) Ti:S laser (Schwartz EO) pumped with a Continuum Verdi G CW laser operating at 532 nm was used. Significant care was taken to remove all extraneous visible light from the illumination beam (see SI_2.3).

2.4 *Multifrequency EPR measurements*

CW X-Band EPR measurements were performed at 5-15 K using a Bruker E500 spectrometer, equipped with an Oxford Instruments ESR 935 cryostat and ITC4 temperature controller. W-band EPR experiments were performed at 4.8 and 7 K using a W-band EPR spectrometer (Bruker ELEXSYS E680) operating at ≈94 GHz, as previously described [44, 45]. A Hahn echo sequence was used to collect the EPR spectra i.e. $t_p - \tau - 2t_p - \tau$–echo. The length of the π/2 microwave pulse was generally set to t_p = 8 ns (S_3 signal) and 40 ns (S_2 signal). The interpulse distance was ≈260 ns.

2.5 *MCD and EPR S-state controls for T. vulcanus PS II*

The PS II samples were very similar to those previously used [32] [46]. The oxygen evolving capacity of the non-recrystallised preparations is typically 3000 μmol of O_2 $(mg\ Chl\text{-}a)^{-1}\ h^{-1}$.
Tris(hydroxymethyl)aminomethane-washed (Tris-washed) PS II samples were prepared by treating the PS II samples with 1 M Tris at pH 8.5 twice at 0.5 mg Chl-a/ml, each with 30 min on ice and precipitated by centrifugation following addition of 12.5% polyethylene glycol. This results in the complete removal of three extrinsic proteins PsbU, PsbV and PsbO, as well as the Mn_4CaO_5 cluster.

The PS II samples used were diluted ≈45% (v/v) with a 1:1 (v/v) mixture of ethylene glycol and glycerol as a glassing agent immediately before use and transferred to a 1 mm path length hydrophobic/lipophobic sample cell. The final PS II concentration (after dilution with glassing agent) of both active and Tris-washed PS II was ≈5mg Chl-a/ml.

The precision of PS II MCD spectral baselines, when utilising the upgraded spectrometer and hydrophobic/hydrophillic sample cells, was established by a comparison with spectra taken at 5 T and -5 T (Fig SI_2.5a). Previously published PS II MCD spectra of *T. vulcanus* in the S_1 state, once corrected for baseline offsets, were seen to be essentially identical to those [32] presented previously (Fig SI_2.5b).

Tris-washed samples show (Fig. SI_2.5c) a reduction in C-term MCD. This is attributable to a loss of cyt c_{550}. In the Tris-washed samples, the structured OEC MCD characteristic in S_1, S_2 and S_3 is absent.

X- and W-band EPR experiments were performed to monitor the behaviour of the same batch of active PS II preparation, in the same glassing mixture and buffer as was used in the optical experiments, albeit at lower concentrations for X-band measurements. S_2 multiline signals were readily obtained from the sample with yields of ≈80%. Yields of S_3, as monitored by the reduction of S_2 multiline intensity upon two saturating YAG laser-flashes were ≈40%. This is comparable to what other workers have obtained [47].

Near-IR illuminations of the S_2 sample at 140 K led to minimal conversion to the S_2-g4 form of S_2, as monitored by the depletion of the S_2 multiline EPR signal at X-band. This is currently attributed to the use of the ethylene glycol/glycerol glassing agent needed for optical experiments. Similarly near-IR illumination of the S_3 state led to minimal yield of any Tyr_Z split signal at W-band.

3 Results

3.1 *S-state dependent PS II MCD overview*

Fig. 1 shows the distinctive changes in MCD spectra occurring upon YAG laser-flash advancing the PS II sample from S_1 to S_2, S_3 and S_0 states. In this series of measurements, the sample was first pre-flashed and dark adapted for 60 minutes at 20^0 C before being cooled to 1.80 K in the spectrometer, to create a well-poised S_1 state. Spectra were recorded at 0 T and at a range of applied magnetic fields. The f0(S_1) spectra in Fig. 1 shows the variation of MCD spectra with magnetic field intensity. The sample was then returned to room temperature in the dark, pre-flashed again and dark-adapted for a further 60 minutes so as to recalibrate the S_1 state, i.e. free of higher S-states and without Tyr_Z oxidation.

The sample was then YAG laser-flashed so as to advance it to S_2 of the Kok cycle. The field dependent measurements for f1(S_2) are shown in Fig.1. This procedure was then repeated to explore the f2(S_3), f3(S_0) and f4(S_1) configurations of the sample (SI_3.2). The same series of measurements, all made on the same sample, also included measurements of f1*(S_2) and f2*(S_3) for which the sample was laser-illuminated at 780 nm (SI_3.2). Finally, the (scrambled) f4(S_1) sample was dark-adapted for 60 minutes and shown to quantitatively reproduce the f0(S_1) spectrum.

Except for the f0(S_1) spectrum, for which the entire PSII sample rests in the S_1 state, subsequent measurements shown in Fig.1 and elsewhere interrogate heterogeneous samples in which a number of S-states are present. The single-flash spectral set of Fig. 1, labelled as f1(S_2), exhibits three narrow features, at 749 nm, 773 nm and 808 nm compared to the two features previously reported [32] in S_1 at 770 nm and 800 nm. The three features in f1(S_2), display the same field dependence and the features can be attributed to the multiline (g=2) form of the S_2 state. As the YAG laser-flash induced yield of S_2 obtained in EPR control experiments has been determined to be ≈ 80%, any residual S_1 MCD component in f1(S_2) spectra is small, especially as the OEC MCD of S_1 is weaker than that of S_2.

Clear, but less dramatic changes in MCD occur when advancing to the f2(S_3) spectrum. The S_2 to S_3 flash-induced transition was also monitored in our samples in EPR. In EPR experiments (Fig. 2), the S_2 to S_3 process was seen to have a yield of ≈40%, as estimated by the loss of the S_2 state; a lower yield for this

step (compared to the S_1 to S_2 step) is mostly due to the accumulation of centres which experience a 'miss', i.e. the percentage of centres advanced per flash is maximally 80%, the maximum two flash yield is 0.8 x 0.8 = 64%. With short (5-10 ns) YAG laser-flashes, 'double hits' are unlikely. We also note that for the sample to advance past S_2, the mobile plastoquinone acceptor Q_B needs to be in its binding pocket.

In the optical experiments, the yield of S_3 is seen to be very similar to that measured in EPR. The S_3 yield in the optical experiment can be estimated from the amplitude of the narrow S_2 MCD features remaining and scaling to the corresponding narrow S_2 features seen in the f1(S_2) spectra. By this method, the S_3 yield (from S_2) is determined to be ≈40%. This value is comparable to that seen (i.e. 46%), for PS II microcrystals prepared from the same material *T. Vulcanus*, reported in the current XFEL S_3 structure [8], as estimated from parallel FTIR measurements.

As the contribution of S_1 to flash-advanced MCD spectra is small, subtracting 60% of f1(S_2) from f2(S_3) provides a pure S_3 MCD spectrum. This spectrum can then be scaled to the magnitude corresponding to a 100% yield of S_3 from S_1. The scaled S_3 spectrum is shown in Fig. 3 and exhibits a slightly broader, blue shifted (-) MCD peak at 764 nm, with a resemblance to the weaker 770 nm peak in S_1 and also to the narrower and stronger 773 nm peak in S_2. The S_2 spectrum in Fig. 3 is also scaled to correspond to a 100 % yield from S_1.

The field dependent behaviour of the S_3 feature in Fig. 1 is distinctly different from that of the S_1 and S_2 features. At 1.80 K the 762 nm S_3 feature approaches saturation between 1 T and 2 T, whereas those of S_2 saturate between 4 T and 5 T.

A first sight, the f3(S_0) MCD spectra in Fig. 2 do not appear to be greatly different to those for f2(S_3). In both, there is a similar shoulder on the remnant of a (narrow) S_2 feature at 773 nm. However, the saturation behaviour of the shoulder near 764 nm in f3(S_0) is different from that of either f1(S_2) or f2(S_3) as seen by the nesting behaviour near 744 nm. The yield from S_2 to S_0 is ≈40%. This relatively high yield, given the S_2 to S_3 yield was similar, can be attributed to the relatively long lifetime of the S_0 state compared to S_3 and the short period (-0.2 s) between the second and third YAG laser-flashes for the f3(S_0) experiment, resulting in negligible S_3 to S_2 decay in this period.

Once the yield of S_0 has been determined, a scaled S_0 spectrum can be obtained from the data in Fig 1. S_0 exhibits a single, relatively broad negative feature peaking with an apparent minimum near 764 nm. Fig. 3 provides the MCD spectra of PS II in the metastable Kok states, S_1, S_2, S_3 and S_0. These spectra were all generated from the same PS II sample and were measured under an identical set of experimental conditions.

3.2 *VTVH MCD spectra*

The temperature dependence of MCD spectra in the near-IR region is shown in Fig 4. These spectra demonstrate the paramagnetic nature of the unstructured MCD at wavelengths longer than 800 nm, present to a very similar extent in each S-state. Such temperature dependent behaviour has been studied previously for S_1 [32] and is due to the high-energy tail of the intense, broad LMCT transitions of oxidised cytochromes which peak near 1600 nm. At wavelengths shorter than 750 nm, Fig. 4 also shows a (smaller)

paramagnetic MCD signal present, as well as a B-term MCD component arising from Chl-a based excitations in PS II and the (minor) PS I content of the sample. The purely temperature dependent component of the MCD is provided by subtracting spectra taken at 1.8 K and 40 K.

The dominantly *paramagnetic* characteristic of the OEC features in S_1 in *T. vulcanus* at temperatures as low as 1.8 K is unexpected. Previous EPR evidence indicated that in spinach, the S_1 state was shown to be weakly diamagnetic [48] [49], having a splitting to a higher lying paramagnetic level of ≈ 2.5 K (1.7 cm^{-1}).

Fig. SI_3.2a presents higher-sensitivity field dependent MCD spectra of PS II poised in f0(S_1) configuration, whilst also extending the range of measurement to applied magnetic fields of 6 T. These low-noise data enable the field dependence for the OEC-based transitions to be distinguished from that due of the tail of the cytochromes. The field dependence of the 770 nm and 800 nm S_1 OEC MCD features was determined graphically, by resolving the fraction of the 5 T spectrum that accurately nulls S_1 OEC-based MCD at other fields. The resulting field dependence is shown in Fig. 5, along with theoretical saturation curves generated using an effective spin Hamiltonian model for the S_1 state (see extended calculations in SI_3.2b), which treats the cluster as a dimer with two antiferromagnetically coupled S=2 components exchange coupled by a parameter J and excludes the fine structure splitting of the Mn ions. The resulting saturation curves are shown in the left hand panel of Fig 5.and are normalised at 5T so as to provide a direct comparison to experimental data.

3.2.1 *S_1 OEC MCD characteristics*

The modelling in Fig. 5 shows that the experimental data for S_1 can be accounted for by using a J value close to -0.2 cm^{-1}. This corresponds to a splitting between the S=0 lowest state and the S=1 first excited state of the cluster of 0.4 cm^{-1}. This is significantly smaller than the value of 1.7 cm^{-1} inferred from the temperature dependence of the EPR of the S_1 state in spinach. Detailed modelling (Fig. SI_3.2b) shows that at temperatures lower than 1.6 K, the difference between weakly diamagnetic J = -0.2 cm^{-1} behaviour and isotropic tanh(gβH/2kT) behaviour becomes easily distinguishable at low fields. Such experiments are feasible and will make quantification of weak diamagnetism more definitive. However as the saturation behaviour seen is indeed similar to that of a g = 2 S = 1/2 system and diverges significantly from the diamagnetic splitting determined from EPR collected in spinach, we cannot not completely exclude the possibility that the 770 nm feature signal arises from a sub-fraction of centres. This may reflect inhomogeneity of the S_1 state or arise from a small population (≈10%) of centres existing in a completely dark stable S_2 state.

3.2.2 *S_2 OEC MCD characteristics*

The S_2 state of PS II is very well studied. S_2 typically can have a high yield of formation and it exhibits a very well structured and distinctive (multiline) EPR spectrum. With its simple S = 1/2, g = 2 characteristic, S_2 VTVH behaviour will arise from the Kramers degeneracy in the ground state and have a tanh(gβH/2kT) form. Both the field dependence and temperature dependence of the MCD closely follow this behaviour. At fields as high as 6 T, there is no evidence for a contribution from higher-lying multiplets

of the exchange-coupled cluster, which have been implicated in modifying effective spin Hamiltonian parameters, leading to enhanced anisotropy. The absence of any contribution from these states is consistent with EPR results in *T. elongatus*, which have indicated [50] that the energy spacing between the ground and excited spin states of the exchange coupled systems is larger (> 10 cm^1) than that seen in higher plants.

The well-structured S_2 MCD features associated with the OEC are stronger than those of S_1. As the yield of S_2 is high (≈80%), a subtraction of f1(S_2) and f0(S_1) spectra provides a good approximation for OEC-based MCD of S_2. Such spectra are provided in Fig SI_3.2c and were used to determine the field dependence in Fig.5 for S2. In Fig SI_3.3a, B-term contributions to the MCD, i.e. from Chl-a absorptions at short wavelengths, are eliminated by the subtraction of corresponding spectra of f1(S_2) and f0(S_1). These B-terms change very little upon flash advancement and can be shown to be almost identical in each step (Fig. SI_3.2c). LMCT MCD C-term features dominate at longer wavelengths, these arise from both oxidised cytochromes The cyt b_{559} signal undergoes small changes upon subsequent YAG laser-flashes and/or freeze/thaw cycles and thus are not completely nulled in difference spectra. As mentioned above, MCD amplitudes in cytochrome-based spectral regions *increase* in older samples, i.e. as cyt b_{559} becomes more oxidised, but cyt b_{559} can also experience reduction. It is known that illumination of PS II samples can lead to cyt b_{559} reduction, presumably due to the production of reduced quinnones, in parallel to OEC oxidation.

There are three distinct features in the S_2 OEC-based components in Fig's. 3 and 4; at 749 nm, 773 nm and 808 nm. The two latter features are similar to features seen in S_1 at 770 nm and 800 nm. The purely temperature dependent component of MCD spectra in f0(S_1) and f1(S_2) are shown as the (offset) spectra in Fig. 4. These reveal a, positive. paramagnetic signal in both S_1 and S_2 extending under the Chl-a based B-terms. A comparison of the purely temperature dependent component of f0(S_1), f0(S_2) and the Tris-washed samples (Fig. 4 and SI_2.4d) establish that such MCD at higher energies is associated with oxidised high-spin Fe(III) cytochromes. The amplitude of the higher energy temperature-dependent component scales well with that of the LMCT band intensity near 900 nm in both f0(S_1), f1(S_2) f2(S_3) and the Tris-washed sample (Fig's. SI_2.5c,d).

When the f1(S_2) sample was illuminated with a 780 near-IR laser at 140 K, to create f1*(S_2), measurable changes were seen in the MCD (Fig. SI_3.2d). Comparing the MCD spectra before and after illumination only small (5-10%) bleach of the S_2 multiline features occurred and a broad negative high-g MCD feature attributable to S_2-g4 was generated at short wavelengths (Fig. SI_3.2e). EPR measurements confirmed a low yield of S_2-g4 in our samples.

3.2.3 *S_3 OEC MCD characteristics*

The f2(S_3) spectra in Fig. 1 exhibit a feature near 760 nm associated with the S_3 state. A systematic subtraction of narrower (associated with S_2) features provides spectra from which a field dependence of the 760 nm S_3 feature can be obtained. The field dependence is shown in Fig. 5, which demonstrates that S_3 state saturates at low magnetic fields, with its initial slope approximately twice that seen for S_2.

The high field (W-band) EPR spectrum can be simulated using a model [44] in which the Mn atoms

couple to form a well-isolated $S = 3$ ground state. In a high spin system, the unpaired spins of all Mn atoms interact by means of both spin-spin and spin-orbit mechanisms. This breaks the degeneracy of the spin mulitplet at zero-field and a fine structure tensor (D) needs to be introduced. The S_3 state EPR data is consistent with the cluster having a small, negative, rhombic zero-field splitting with $D \approx 0.2$ cm^{-1}. This relatively small value is consistent with the cluster having four octahedrally coordinated Mn(IV) ions.

The magnetic saturation properties of MCD signal(s) provide additional information, not accessible by EPR. MCD saturation curves depend on the (ground state) spin Hamiltonian terms mentioned above and additional terms associated with the *product* of transition moment vector components $M_{x,y,z}$, between the ground sate and the *electronic* excited state. Fig. 5 shows that MCD associated with YZ i.e. M_y,M_z polarisation product, reproduces the saturation of S_3 seen in the 1.8 K experiment. A determination of the (small) D values in octahedral Mn(IV)s is in principle accessible by means of MCD saturation measurements taken at increasingly low fields and temperatures. Saturation curve nesting, as seen in Fig. SI_3.2b, which shows modelling of the weak diamagnetism of S_1, is an example of the type of behaviour that could lead to an independent determination of the D parameter. The yield-corrected S-state spectra in Fig. 3 point to a broader negative component(s) associated with S_3, in the 780 nm to 850 nm region. These broader component(s) have the same (high-spin) saturation behaviour as the main feature.

When the f2(S_3) sample was illuminated using 775 nm near-IR laser light at 1.8 K, significant spectral changes occurred (Fig. SI_3.2f). A comparison of MCD spectra taken before and after illumination (Fig. SI_3.2g) reveal the 20-25% bleach of g=2, S_2 multiline features. A broad positive high-g MCD feature is created at short wavelengths. No measureable change is seen in the S_3 component. In EPR control measurements, there was only a small Tyr_Z-like split signal seen. There were some small changes in the (broad) EPR signals associated with the S_3 state. Being able to have samples that have substantial near-IR activity in both S_2 and S_3 is a priority for future work.

3.2.4 *S_0 OEC MCD characteristics*

The S_0 state of PS II is not as well studied as other S-states, even though S_0 is an odd electron configuration and nominally well-suited to the EPR technique [51, 52] [53, 54]. Well-structured S_0 EPR spectra can be obtained from cyanobacterial PSII samples and in spinach samples when methanol is added. There is little doubt that our f3(S_0) spectrum has advances with good yield to S_0 as the [f3(S_0)-f2(S_3)] spectrum closely replicates an inverted S_3 spectrum.

Fig. SI_3.2h shows the field dependent spectra of f3(S_0), corrected for the S_2 and S_3 components. At first sight, it appears that the OEC of S_0 may exhibit a relatively broad negative MCD signal, evident as a peak near 755 nm. However, this is deceiving. The field dependence of MCD in this region in S_0 is *not* paramagnetic. It manifests as a *linear* signal (B-term) to within experimental error (Fig.SI_3.2j).

The top panel of Fig. SI_3.2i displays step-wise changes of S_0 MCD upon each 1 T increase in applied field. For the final (5 T-4 T) step, the cytochrome MCD contribution becomes small as its C-term based intensity is close to saturation. The B-term component associated with each step, owing to Chl-a bands is present, as it is for the other S-states. However, there is a broad negative component extending from 710

nm to ≈900 nm that increases linearly with field. This B-term activity is seen clearly in the field dependence of S_0-S_1 spectra (SI_3.2j, lower panel) in which B-terms associated with Chl-a are eliminated and signals due to cytochrome are strongly reduced. The temperature dependence of the MCD of f3(S_0) also displays a very broad negative signal near 755 nm up to 40 K, this being consistent with the B Term nature of this band.

When the f4(S_1) spectrum is compared to that of f3(S_0) (SI), it is evident that the negative MCD B-term associated with S_0 is reduced (Fig. SI_3.2k), indicating that a significant fraction of S_0 advances to S_1. The f4(S_1) spectrum can be attributed to ≈50% S_2, 10% S_3 and ≈10% S_0, with the remainder (≈30%) being S_1. There are no identifiable OEC based MCD features in the S_0 with VTVH behaviour similar to those seen for S_1, S_2, and S_3. The very broad and featureless negative B-term MCD appears to be unique to S_0.

3.3 Determining OEC-based spectra of each S-state

A comparison of S-state MCD spectra in Fig. 3 along with the temperature dependent data in Fig. 4 help discriminate between features due to S-state advancement within the OEC and those due to other cofactors of PS II. There is minimal change in B-terms associated with Chl-a components of PS II in the advancement process (Fig. SI_3.2c). However, strong C-term signals associated with high-spin Fe(III) cytochromes underlie both OEC-based signals as well the Chl-a-based B-term components. Cytochrome-based signals are variable and change with both thermal cycling and YAG-flashing of the sample.

Cytochrome-based MCD changes are less problematic for the S_2, state as the yield is high (≈ 80 %). S_2 OEC-based MCD features are narrow and can be identified against a cytochrome background (Fig SI_3.3a. For S_3, where yields are lower and where OEC-based features in S_2 and S_3 overlap, alternative procedures are needed to reliably extract an OEC-based S_3 MCD spectrum.

One approach is to use the distinctly different saturation behaviour seen for S_2 and S_3 (Fig. 5). Comparing double difference spectra and taken between the f2(S_3) spectra and f1(S_2) spectra at 6 T, where both S_2 and S_3 are saturated and those taken at 2 T where only S_3 is saturated allows extraction of an OEC-based S_3 spectrum (see Fig. SI_3.3b), independent of any estimate of the yield of S_3.

A second procedure that leads to less noisy spectra, is to use the yield of S_3, as determined via a graphics-based determination of the magnitude of the narrow and distinctive S_2 features remaining in f2(S_3) spectra to determine the OEC-based profile of S_3. A comparison of S_3 profiles determined by these procedures is provided in Fig. SI_3.3b. Both procedures lead to similar very lineshapes and amplitudes. The yield-based spectrum, determined by difference spectra taken at 2 T as well as the saturation-based spectrum are less prone to errors but are noisier.

The S_0 OEC-based spectrum, having B-term behaviour, is easily distinguishable from other S-states. Once the Chl-a B-term component is accounted for, the S_0 OEC-based profile can be distinguished from both cytochrome signals and other S-state OEC-based components, which become largely saturated at 5 T and 1.8 K.

Having determined OEC-based S-state MCD profiles of S_2 and S_3 using the procedures above, it becomes possible to reliably model both the Chl-a and cytochrome MCD components by fitting these (with

3rd order polynomials) to the yield-corrected experimental data, and subsequently subtract these interfering components. Fig. 6 demonstrates this analysis for S_2.

The fitted curves for cytochrome and Chl-a components determined in Fig. 6 can, with only minor amplitude changes of the components associated with changes in individual sample concentrations and fraction of oxidised cytochromes, can be used to generate OEC-based MCD spectra of the other S-states. The complete set of OEC-based spectra is shown in Fig. 7. These data have better signal to noise than those generated by double differences etc., and as the spectra contains no components due to PS I, can be put on a PS II molar extinction scale. The narrow S-state dependent features have a $\Delta\varepsilon$ between 0.5 and 4 M^{-1} cm^{-1} at 5 T and 1.8 K.

3.4 *Narrow Mn(IV) features in the Near-IR MCD of Model Compounds*

Weak, narrow MCD features, assigned to $^4A \rightarrow {}^2E$ spin forbidden transitions of Mn(IV) have been reported[55] in the near-IR region for a number of Mn(III)-Mn(IV) μ-oxo bridged dimers. These dimers served to model MnCat, which is an enzyme that is structurally related to the OEC. The data in Fig. 8 (see SI_3.4 for details) reproduced measurements on $[Mn_2O_2(bpy)_4]^{3+}$ at higher sensitivity, as well as providing data on a more recent synthesised MnCat model, DNTE [56]. The latter dimer exhibits a weak narrow band at 880 nm. Also shown in Fig. 8 are MCD measurements of the Mn cubane oligomer cubium$^+$, which serves as a model compound for the OEC [57]. This system exhibits *two* narrow MCD features, at 683 nm and 709 nm. This observation is consistent with there being two distinct Mn(VI)s in this system.

4 Discussion

4.1 *Spectral Assignments and the Nephelauxetic Effect*

A key characteristic of the OEC S-state dependent MCD spectra in the S_1, S_2 and S_3 states is that they exhibit features with FWHM widths of only 10-20 nm FWHM (Table 1).

These bands are far narrower than spin-allowed d-d bands of Mn(III) or Mn(IV) which typically have widths 10-20 times larger. Many spin-forbidden bands are also comparably broad. However, the exception is spin-flip d-d bands, which represent inversions of a single spin *within a single orbital configuration* and are, by contrast, narrow.

The lowest-energy orbital configuration of the octahedral d^3 ion is $t_{2g}{}^3$. The lowest energy term is then ^4A_g, in which each of the three t_{2g} electrons are parallel. The first excited state is ^2E_g and it has the *same* orbital configuration as the ground state, $t_{2g}{}^3$, with one electron spin 'flipped'. This excitation derives its energy from the change in electron repulsion amongst the t_{2g} electrons upon inverting a spin and is affected little by energy changes in low symmetry splittings of t_{2g} and e_g orbitals (which are determined by ligand fields). As the orbital configuration in a spin-flip excitation is not changed, there is little nuclear displacement between the ground and excited state. Consequently, the dominant intensity resides in the *purely electronic* excitation with little intensity occurring in vibrational sidelines. This purely electronic nature ensures spin-flip excitations narrow.

Although spin-flips are ligand-field independent, it was recognised long ago that their excitation energy varied significantly with the nature of the ligands co-ordinating the metal [58]. F^- coordination led to excitation energies closest to that of the corresponding atomic, gas phase excitation of the free ion whilst Cl^-, NH_3 or I^- coordination lead to a gradual reduction of the spin-flip excitation energy. This nephelauxetic effect was attributed to the 'hard' or 'soft' nature of ligands and specifically to their 'cloud-expanding' effect on d-orbitals. The simplistic rationale is that electronic wavefunction delocalisation leads to a reduction of the d-electron repulsion terms that define the spin-flip energy. The nephelauxetic effect is larger for metals of higher valence. This is clearly shown in a series of d^2 systems with increasing metal charge [59]. Nephelauxetic effects in Mn(IV) complexes are thus larger than those in equivalent Mn(III) systems.

For Mn(IV) in a crystalline F^- environment, sharp $^2E \rightarrow {}^4A$ emission occurs near 623 nm [60]. Mn(IV) doped oxides exhibit $^2E \rightarrow {}^4A$ emission over the 700 nm -720 nm range [61]. For Mn(IV) an octahedral O-(SeO_4) environment in $Mn(SeO_4)_2$, the same transition occurs at 755 nm [62]. MCD spectra of the monomeric Mn(IV) complex molecular $[MnIV(OMe)_3(Me_3TACN)]^+$ reports [63] a spin-flip feature at 715 nm. Very recently, $^2E \rightarrow {}^4A$ emission of a *bis*-(tris(carbine) borate) complex of Mn(IV) which has C-(carbine) coordination has been reported [64] at 828 nm.

Spin-flip transitions for both Mn(III) and Mn(IV) are well documented in a series of molecular oxo-bridged dimer model compounds of MnCat[55]. The Mn(III) spin-flips occur in the 500 nm - 550 nm spectral region, whereas Mn(IV) spin-flips occur near 806 nm, the latter having widths of ≈10-20 nm. We have repeated measurements on the $[Mn_2O_2(bpy)_4]^{3+}$ dimer and made measurements of an additional dimer, DTNE. These data are shown in Fig. 8 and our measurements for the former system confirm the previous experimental results

The examples above establish that the $^4A \rightarrow {}^2E$ spin-flip in Mn(IV) systems occur in the range 620 nm to 880 nm. Although the overall trend is clear, with F^- ligands leading to the highest energy case and other ligands lower, it is not immediately clear why cubium$^+$ with both P-(phosphinate) and O-(cubane-oxo bridge) ligating atoms has spin-flips at quite high energy nor why the $[MnIV(OMe)_3(Me_3TACN)]^+$ complex with three N-(TACN) and three O-(OMe) ligating atoms has a higher energy transition than $Mn(Se0_4)_2$ which has six O-(SeO_4) ligating atoms.

A recent review on the nephelauxatic effect [65] has reiterated the point that there are clear anomalies in attributing the effect simply to delocalisation of d electrons. An alternative approach is to attribute the effect to the polarisability of ligands rather than delocalisation. A differential nephelauxetic effect has been reported between t_2 and e orbitals [66]. This work also indicates a quasi additivity of the nephelauxetic shift in a series of hexadentate complexes in which the ratio of ligating N to S atoms is varied. A beautiful example of a quasi-additivity of shifts is provided by the study of series of mixed Ni(II) doped bromides/chlorides[67]. An analysis of the relativistic nephelauxetic effect establishes that spin orbit coupling on a metal can be significantly reduced [68] via this process.

Spin-flips in the Mn_4CaO_5 cluster (Table 1) occur over a relatively part of this overall range seen for the Mn(IV) systems discussed above. The data in Table 1 show two similar energy peaks in both S_1 and S_2 i.e. at ≈ 770 nm and ≈ 800 nm. These are provisionally assigned to the Mn2 and Mn3 atoms of the cluster, as they do not change their valence in passing from S_1 to S_2 within the dominant OEC model. The additional sharp positive peak created at 749 nm in S_2, is then assigned to Mn4. More definitive assignments would be greatly assisted by MCD measurements on the near-IR illuminated forms of S_2 and S_3. Our samples showed low yields of these conversions (SI_3.2). The S_2-g4 state shows the emergence a broad putatively Mn(III) d-d band, which could then be associated with Mn4, but more detailed spectra are required.

4.2 *Magnitude and sign of spin-flip MCD*

The rationale in 4.1 points to an assignment, based on energetics, bandwidths and model compounds, which confirm the narrow bands seen in OEC MCD of the PS II in the 710 nm-800 nm region as spin-flips of Mn(IV)s. The spin-flip absorption intensity for an *isolated* Mn(IV) species (not magnetically coupled to other ions) is weak, gaining intensity through spin-orbit coupling to spin-allowed transitions. The $^4A \rightarrow {}^2E$ spin-flip, which can be extremely sharp in some systems, is often only seen in emission. It is far more difficult to see in absorption. We know of no magnetically isolated Mn(IV) system in which a $^4A \rightarrow {}^2E$ spin-flip has been clearly identified in absorption.

In PS II and in the model compounds of MnCat, spin-flips are clearly visible in MCD. At low temperature and high field conditions, the molar extinction is in the range $\Delta\varepsilon$=0.1-3 M^{-1} cm^{-1} (Table 1). Absorption cannot be greater than 2xΔA as by definition, $\Delta A = A_L - A_R$ and $A = (A_L + A_R)/2$. Thus PS II spin-flips must have ε >0.2 M^{-1} cm^{-1}. The ratio $\Delta A/A$ >0.1 in MCD is rarely exceeded, and ε is likely to be ≈2 M^{-1} cm^{-1} or higher. Even at this intensity, the absorbance due to the OEC in our sample would not exceed $5x10^{-5}$ and thus be significantly weaker than vibrational overtone features exhibited by the sample.

The relatively strong absorption intensity implied from the intensity of MCD in PS II (and MnCat model compounds) for Mn(IV) spin-flips, arises from the magnetic exchange-coupled electric dipole mechanism [69]. This process is known to dramatically enhance spin-forbidden absorption by compensating the spin change upon electronic excitation of one metal centre by simultaneously changing the spin level of the exchange coupled dimer (or cluster), so that the *total* $\Delta S=0$ spin selection rule for optical excitation is preserved [70].

The absorption mechanism and thus MCD associated with such an exchange-coupled enhanced absorption process is quite distinct from that arising from the normal, single-centre (spin-orbit mixing with spin-allowed states) process. A summary of some of the concepts involved is given in SI_4.2. The consequences of the exchange-coupled mechanism are that not only the *intensity* of a spin-flip absorption dramatically increases, but also that the relative magnitude of MCD to absorption ($\Delta A/A$) can vary. Even the *sign* of the MCD can reverse.

The VTVH MCD behaviour exhibited in magnetically-coupled systems is inherently complex but also is both distinctive and informative. In PS II, each Mn in the Mn_4CaO_5 cluster is coupled to the other Mn

atoms via exchange parameters |J| of the order of 0.1-50 cm^{-1} and the coupling can be either ferromagnetic (J>0) or antiferromagnetic (J<0). These couplings lead to a (magnetic) ground state of the cluster having a particular net total spin value in its lowest magnetic state. This spin value is often determinable through EPR measurements. There will also be a number of (magnetically) excited states of the cluster in which the total spin changes, and these will become populated at higher temperatures. In our MCD measurements, the applied magnetic field is varied between 0 and 6 T. This can lead to Zeeman shifts that are larger than the energy separations in the exchange coupled ladder of the cluster. Zeeman shifts can lead to spin sub-levels of higher excited states being populated at 1.8 K or even becoming the lowest state. An example of this type of behaviour is given in our analysis of the S_1 state, where J=-0.2 cm^{-1}. The system is nominally diamagnetic but becomes effectively paramagnetic in fields > 0.2 T.

An instructive example of the influence of magnetic exchange coupling on MCD is provided by the study [16] reported for three isomorphous molecular dimers containing two metal ions. The metal dimers are **I** Cr(III)-Zn(II), **II** Gd(III)-Ni(II), **III** Cr(III)-Ni(II). Zn(II) and Gd(III) are diamagnetic, absorbing minimally through the visible spectral region. Spectra of **I** and **II** report the d-d MCD of magnetically isolated Cr(III) and Ni(II). The MCD of **III** is *not* however a simple sum of MCD spectra of **I** and **II**. Using a spin Hamiltonian model, the authors are able to account *fully* for the (complex) VTVH MCD of **III**, from magnetic properties of **I** and **II** along with the magnetic susceptibility of **III**.

Two observations from this study are immediately pertinent to our work. In **I**, which has a magnetically isolated Cr(III), the $^4A \rightarrow {}^2E$ transition (which is isoelectronic to the spin-flip in Mn(IV)) is not visible in absorption or MCD. In the exchange coupled dimer **III** the Cr(III) spin-flip appears as a narrow (≈15 nm) FWHM feature, with $\Delta\varepsilon \approx 0.5$ M^{-1} cm^{-1} under saturating conditions. Both the width and MCD intensity of the Cr(III) spin-flip parallel the behaviour seen for Mn(IV) spin-flips seen in PS II.

A second relevant characteristic of this work is that the MCD of the lowest energy spin-allowed Ni(II) transition (the $^3T_2$ manifold) changes in *both sign and magnitude* in going from the isolated case **II** to the exchange-coupled case **III**. The VTVH behaviour of **III** is described as 'stunningly complex'. A synopsis of the phenomenon is that a) the amplitude and non-linear VTVH behaviour of MCD seen for d-d transitions in open shell metal systems depends critically on spin-orbit coupling at the metal centre undergoing the excitation. b) Magnetic coupling of a particular metal centre to other magnetic ion(s) can serve to alter both the *magnitude and direction* of spin experienced at the centre, i.e. its spin projection. This change in spin projection can then manifest in changes in the MCD magnitude, as well as sign. The spin-Hamiltonian analysis also requires the exchange coupling in the excited state to be incorporated, as well as the direction and magnitude of the electronic transition moments.

In PS II, each Mn(IV) will experience a particular projection of the cluster total spin, relative to its (local) transition moment directions. This will vary with S-state. Each Mn(IV) spin-flip will have an absorption strength (and direction of its optical transition dipoles) according to the effectiveness of the exchange coupling processes that overcome the spin-forbidden nature of the transition. Measurements of

the intensity and sign of each individual spin-flip can then provide, through an appropriate analysis, details of the exchange coupling components within the cluster.

5 Conclusions

MCD measurements in the near-IR region of PS II cores of *T. vulcanus,* between 710 nm and 900 mm, are shown to provide a distinctive optical signature in each metastable S-state. Each S-state has its own MCD spectral profile as well as VTVH behaviour. This new window provides valuable information on both the electronic structure of and magnetic coupling within the Mn_4CaO_5 cluster as it transits through the catalytic Kok cycle of water oxidation.

There remains little doubt that the narrow features seen for OEC based MCD are due to $^4A \rightarrow {}^2E$ spin-flips of Mn(IV) ions. The sign, magnitude and field dependence of these features depend on rather complex aspects of exchange coupling within the Mn_4CaO_5 cluster. Modelling of the relative positions of the $^4A \rightarrow {}^2E$ bands by utilising computational chemistry techniques [71] needs to be developed. This will help identify the detailed local nature of each Mn(IV). However, modelling the sign, magnitude and general VTVH behaviour may require an extension of the (dimer) spin-Hamiltonian model to a cluster model. A significant number of parameters may need to be derived computationally.

The weak diamagnetism seen for the S_1 state, analysed to have a paramagnetic level ≈ 0.4 cm^{-1} above the diamagnetic ground state, compares to a value of 1.7 cm^{-1} reported from EPR measurements using PS II sourced from spinach. The lack of any 'spin-flip' or other paramagnetic OEC based feature in S_0 MCD does not exclude the presence of a Mn(IV) in S_0 as it may be either significantly weaker and/or lie outside the optical window available.

We see no evidence for any broad, temperature-dependent transitions in any of our (non-IR illuminated) OEC based MCD spectra, at a sensitivity level of $\approx \Delta\varepsilon$ of 0.06 M^{-1} cm^{-1} under saturation conditions. If present in the 710 nm - 850 nm region, one would expect to be able to see spin-allowed MCD of d-d transitions of Mn(III). This implies that low symmetry d-orbital splittings of Mn(III), which are responsible for the bands seen in the 700 nm -800 nm region of the MnCat systems and model compounds, are at higher energies in *T. Vulcanus* PS II.

Our assignment of two and three spin-flips, and thus at least two or three Mn(IV) sites in S_1 and S_2 states respectively, is consistent with the dominant 'high-paradigm' model [72] [73] [44] [7, 74] of the OEC. EPR changes induced by near-IR illumination of S_2 or S_3 states may now considered to be influenced by excitation spin-forbidden excitations of Mn(IV)s.

Having established the feasibility and utility of S-state dependent MCD spectroscopy, now heralded is the opportunity to make parallel S-state dependent MCD measurements on any of the wide range of *modified* PS II core preparations, especially those targeting the critical and malleable S_3 state. MCD measurements of PS II derived from other organisms will also be invaluable. An immediate example would be to study S_1 in *Synechosystis sp.* PCC 6803, where highly structured EPR has been reported [75]. Another would be to measure S_0 MCD in a sample in which methanol has been added. Methanol has been shown to significantly affect the S_0 EPR of spinach [51].

Acknowledgements

The technical support of Keith Jackman is again gratefully acknowledged. E.K. gratefully acknowledges correspondence with Bill Rutherford, Daniel Gamellin, Thomas Brunold, Hans Güdel, Andreas Hauser, Christian Reber, Ron Pace, Rob Stranger and Mark Riley. We recognise the support of the Australian Research Council through grants DP110104565 and DP 150103137 (E.K.), FT140100834 (N.C) and MEXT/JSPS of Japan through a Grant-in-Aid for Specially Promoted Research No. 24000018 (J.R.S.).

Figure Captions

Figure 1:
The four panels show the field dependence of the MCD of T. vulcanus at 1.80 K, utilising a pre-flash followed by 60 minute dark adaption before 0, 1, 2 or 3 YAG laser-flashes (see text). $\Delta A=10^{-5}$ corresponds to $\Delta\varepsilon$ of $\approx 0.6\ M^{-1}\ cm^{-1}$ for PS II.

Figure 2:
EPR control measurements of the OEC in PS II of T. vulcanus were performed at both W-band, right hand panel, (94 GHz) and X-band, left hand panel, (9 GHz). The right hand panel shows the f2(S_3)-f1(S_1) difference spectrum at W-band (magenta) at 4.8 K as well as the simulated spectrum (black curve). The parameters used in the simulation were those of reference [44], g=1.99, S=3, D=0.175 cm-1, E/D=0.27. Turning points of the S_3 state signal (S=3) are marked in blue. An additional Mn_4O_5Ca signal is also observed near 2 T marked as ? which may be due to the influence of the cryoprotectant. Assignment of this feature forms a part of ongoing work. The left hand panel shows the 8 K (S_2 multiline) spectra,for singly doubly and triply flashed samples as indicated. The doubly flashed sample f2(S_3) (magenta) has an S_2 multiline amplitude of 52% of the singly flashed sample f1(S_2) (green) and that of the triply flashed sample f3(S_0) (cyan) falls to 35 %.

Figure 3:
Scaled Near-IR MCD spectra of PS II for each S-state. The regions dominated by Chl-a (<730 nm), the OEC (730 nm-820 nm) and cyt b_{550}/cyt c_{550} (>820 nm) are annotated.

Figure 4:
MCD at 5 T of PS II of T. vulcanus for the samples YAG laser-flashed advanced to S_1, S_2 and S_3. S-states of PS II (see text) the temperatures indicated. The offset (magenta) curves are the difference between spectra taken at 1.8 K and 40 K. Temperature dependent spectra were taken of different samples to the one used in Fig. 1. These latter samples had been thermally cycled more often and exhibited slightly lower yields of S_2 and S_3 as well as exhibiting an increased fraction of oxidised cyt b_{559}. Apart from amplitude, the spectral characteristics of S_1, S_2 and S_3 were mot measurably different and differences do not affect the interpretation of data.

Figure 5:
The magnitude of the field dependence of the 770 nm MCD feature of T. vulcanus in the S_1 state at 1.8 K (left hand panel), compared to theoretical curves (see text) for J=0, -0.1, -0.2, -0.3, -0.4, -0.5 and -0.85 cm^{-1}, normalised at 5 T. Analogous saturation curves for the S_2 and S_3 states are shown in the right hand panel as well as theoretical saturation curves for an isotropic g=2, S=1/2 doublet (green) appropriate to S_2 and using the same parameters as used for the simulation of the W-band EPR of S_3 (magenta) used in Fig. 2.

Figure 6:

Near-IR MCD of the S_2 state (green) together with fits to the cytochrome (red) and Chl-a (blue) components (see text). The residual OEC-based S_2 MCD, after these fitted components have been subtracted, is also shown (dotted black).

Figure 7: *Calibrated OEC-based near-IR MCD spectra at 5 T and 1.8 K for the S-states of PS II.*

Figure 8:
Near-IR MCD spectra of model compounds exhibiting narrow MCD features (see SI 3.4 for experimental details). Spectra are on the same ordinate scale as Figs. 6 & 7 whilst being extended (yellow shaded region) to where MCD measurements are precluded in PS II by intense Chl-a based pigment absorptions. For comparison purposes, the green dotted line is the OEC-based MCD of the S_2 state of PS II taken from Fig. 7 (MCD not to scale).

References

[1] Y. Umena, K. Kawakami, J.R. Shen, N. Kamiya, Crystal structure of oxygen-evolving photosystem II at a resolution of 1.9 angstrom, Nature, 473 (2011) 55-U65.

[2] M. Suga, F. Akita, K. Hirata, G. Ueno, H. Murakami, Y. Nakajima, T. Shimizu, K. Yamashita, M. Yamamoto, H. Ago, J.R. Shen, Native structure of photosystem II at 1.95 A resolution viewed by femtosecond X-ray pulses, Nature, 517 (2015) 99-103.

[3] J.P. McEvoy, G.W. Brudvig, Water-splitting chemistry of photosystem II, Chemical Reviews, 106 (2006) 4455-4483.

[4] N. Cox, D.A. Pantazis, F. Neese, W. Lubitz, Biological Water Oxidation, Accounts of Chemical Research, 46 (2013) 1588-1596.

[5] J.R. Shen, The Structure of Photosystem II and the Mechanism of Water Oxidation in Photosynthesis, Annu Rev Plant Biol, 66 (2015) 23-48.

[6] B. Kok, B. Forbush, M. Mcgloin, Cooperation of Charges in Photosynthetic O2 Evolution .1. A Linear 4step Mechanism, Photochemistry and Photobiology, 11 (1970) 457-&.

[7] M. Perez-Navarro, F. Neese, W. Lubitz, D.A. Pantazis, N. Cox, Recent developments in biological water oxidation, Curr Opin Chem Biol, 31 (2016) 113-119.

[8] M. Suga, F. Akita, M. Sugahara, M. Kubo, Y. Nakajima, T. Nakane, K. Yamashita, Y. Umena, M. Nakabayashi, T. Yamane, T. Nakano, M. Suzuki, T. Masuda, S. Inoue, T. Kimura, T. Nomura, S. Yonekura, L.J. Yu, T. Sakamoto, T. Motomura, J.H. Chen, Y. Kato, T. Noguchi, K. Tono, Y. Joti, T. Kameshima, T. Hatsui, E. Nango, R. Tanaka, H. Naitow, Y. Matsuura, A. Yamashita, M. Yamamoto, O. Nureki, M. Yabashi, T. Ishikawa, S. Iwata, J.R. Shen, Light-induced structural changes and the site of O=O bond formation in PSII caught by XFEL, Nature, 543 (2017) 131-+.

[9] I.D. Young, M. Ibrahim, R. Chatterjee, S. Gul, F.D. Fuller, S. Koroidov, A.S. Brewster, R. Tran, R. Alonso-Mori, T. Kroll, T. Michels-Clark, H. Laksmono, R.G. Sierra, C.A. Stan, R. Hussein, M. Zhang, L. Douthit, M. Kubin, C. de Lichtenberg, L.V. Pham, H. Nilsson, M.H. Cheah, D. Shevela, C. Saracini, M.A. Bean, I. Seuffert, D. Sokaras, T.C. Weng, E. Pastor, C. Weninger, T. Fransson, L. Lassalle, P. Brauer, P. Aller, P.T. Docker, B. Andi, A.M. Orville, J.M. Glownia, S. Nelson, M. Sikorski, D.L. Zhu, M.S. Hunter, T.J. Lane, A. Aquila, J.E. Koglin, J. Robinson, M.N. Liang, S. Boutet, A.Y. Lyubimov, M. Uervirojnangkoorn, N.W. Moriarty, D. Liebschner, P.V. Afonine, D.G. Waterman, G. Evans, P. Wernet, H. Dobbek, W.I. Weis, A.T. Brunger, P.H. Zwart, P.D. Adams, A. Zouni, J. Messinger, U. Bergmann, N.K.

Sauter, J. Kern, V.K. Yachandra, J. Yano, Structure of photosystem II and substrate binding at room temperature, Nature, 540 (2016) 453-+.

[10] C. Kupitz, S. Basu, I. Grotjohann, R. Fromme, N.A. Zatsepin, K.N. Rendek, M.S. Hunter, R.L. Shoeman, T.A. White, D.J. Wang, D. James, J.H. Yang, D.E. Cobb, B. Reeder, R.G. Sierra, H.G. Liu, A. Barty, A.L. Aquila, D. Deponte, R.A. Kirian, S. Bari, J.J. Bergkamp, K.R. Beyerlein, M.J. Bogan, C. Caleman, T.C. Chao, C.E. Conrad, K.M. Davis, H. Fleckenstein, L. Galli, S.P. Hau-Riege, S. Kassemeyer, H. Laksmono, M.N. Liang, L. Lomb, S. Marchesini, A.V. Martin, M. Messerschmidt, D. Milathianaki, K. Nass, A. Ros, S. Roy-Chowdhury, K. Schmidt, M. Seibert, J. Steinbrener, F. Stellato, L.F. Yan, C. Yoon, T.A. Moore, A.L. Moore, Y. Pushkar, G.J. Williams, S. Boutet, R.B. Doak, U. Weierstall, M. Frank, H.N. Chapman, J.C.H. Spence, P. Fromme, Serial time-resolved crystallography of photosystem II using a femtosecond X-ray laser, Nature, 513 (2014) 261-+.

[11] S.B. Piepho, P.N. Schatz, Group Theory in Spectroscopy with Applications to Magnetic Circular Dichroism, Wiley-Interscience, New York, Chichester, Brisbane, Toronto, Singapore, 1983.

[12] N. Cox, J. Messinger, Reflections on substrate water and dioxygen formation, Bba-Bioenergetics, 1827 (2013) 1020-1030.

[13] L. Rapatskiy, N. Cox, A. Savitsky, W.M. Ames, J. Sander, M.M. Nowaczyk, M. Rogner, A. Boussac, F. Neese, J. Messinger, W. Lubitz, Detection of the Water-Binding Sites of the Oxygen-Evolving Complex of Photosystem II Using W-Band O-17 Electron-Electron Double Resonance-Detected NMR Spectroscopy, Journal of the American Chemical Society, 134 (2012) 16619-16634.

[14] P.N. Schatz, R.L. Mowery, E.R. Krausz, MCD/MCPL [Magnetic CD/magnetic circularly polarized luminescence] saturation theory with application to molecules in Dh and its subgroups, Mol. Phys., 35 (1978) 1537-1557.

[15] E.I. Solomon, M.L. Neidig, G. Schenk, 2.26 - Magnetic Circular Dichroism of Paramagnetic Species, in: J.A. McCleverty, T.J. Meyer (Eds.) Comprehensive Coordination Chemistry II, Pergamon, Oxford, 2003, pp. 339-349.

[16] S. Piligkos, L.D. Slep, T. Weyhermuller, P. Chaudhuri, E. Bill, F. Neese, Magnetic circular dichroism spectroscopy of weakly exchange coupled transition metal dimers: A model study, Coordination Chemistry Reviews, 253 (2009) 2352-2362.

[17] A. Boussac, J.J. Girerd, A.W. Rutherford, Conversion of the spin state of the manganese complex in photosystem II induced by near-infrared light, Biochemistry, 35 (1996) 6984-6989.

[18] A. Boussac, H. Kuhl, S. Un, M. Rogner, A.W. Rutherford, Effect of near-infrared light on the S-2-state of the manganese complex of photosystem II from Synechococcus elongatus, Biochemistry, 37 (1998) 8995-9000.

[19] A. Boussac, S. Un, O. Horner, A.W. Rutherford, High-spin states (S >= 5/2) of the photosystem II manganese complex, Biochemistry, 37 (1998) 4001-4007.

[20] D.A. Pantazis, W. Ames, N. Cox, W. Lubitz, F. Neese, Two Interconvertible Structures that Explain the Spectroscopic Properties of the Oxygen-Evolving Complex of Photosystem II in the S2 State, Angew Chem Int Edit, 51 (2012) 9935-9940.

[21] H. Isobe, M. Shoji, S. Yamanaka, Y. Umena, K. Kawakami, N. Kamiya, J.R. Shen, K. Yamaguchi, Theoretical illumination of water-inserted structures of the CaMn4O5 cluster in the S-2 and S-3 states of oxygen-evolving complex of photosystem II: full geometry optimizations by B3LYP hybrid density functional, Dalton T, 41 (2012) 13727-13740.

[22] N. Cox, F.M. Ho, N. Pewnim, R. Steffen, P.J. Smith, K.G.V. Havelius, J.L. Hughes, L. Debono, S. Styring, E. Krausz, R.J. Pace, The S-1 split signal of photosystem II; a tyrosine-manganese coupled interaction, Bba-Bioenergetics, 1787 (2009) 882-889.

[23] N. Ioannidis, G. Zahariou, V. Petrouleas, Trapping of the S-2 to S-3 state intermediate of the oxygen-evolving complex of photosystem II, Biochemistry, 45 (2006) 6252-6259.

[24] Y. Sanakis, N. Tagmatarchis, E. Aslanis, N. Ioannidis, V. Petrouleas, H. Shinohara, K. Prassides, Dual-mode X-band EPR study of two isomers of the endohedral metallofullerene Er@C-82, Journal of the American Chemical Society, 123 (2001) 9924-9925.

[25] K.G.V. Havelius, J.H. Su, Y. Feyziyev, F. Mamedov, S. Styring, Spectral resolution of the split EPR signals induced by illumination at 5 K from the S-1, S-3, and S-0 states in photosystem II, Biochemistry, 45 (2006) 9279-9290.

[26] K.G.V. Havelius, J.H. Su, G. Han, F. Mamedov, F.M. Ho, S. Styring, The formation of the split EPR signal from the S-3 state of Photosystem II does not involve primary charge separation, Bba-Bioenergetics, 1807 (2011) 11-21.

[27] A. Boussac, M. Sugiura, T.L. Lai, A.W. Rutherford, Low-temperature photochemistry in photosystem II from Thermosynechococcus elongatus induced by visible and near-infrared light, Philos T R Soc B, 363 (2008) 1203-1210.

[28] A. Boussac, M. Sugiura, D. Kirilovsky, A.W. Rutherford, Near-infrared-induced transitions in the manganese cluster of photosystem II: Action spectra for the S-2 and S-3 redox states, Plant and Cell Physiology, 46 (2005) 837-842.

[29] S.R. Cooper, M. Calvin, Mixed-Valence Interactions in Di-Mu-Oxo Bridged Manganese Complexes, Journal of the American Chemical Society, 99 (1977) 6623-6630.

[30] S.R. Cooper, G.C. Dismukes, M.P. Klein, M. Calvin, Mixed-Valence Interactions in Di-Mu-Oxo Bridged Manganese Complexes - Electron-Paramagnetic Resonance and Magnetic-Susceptibility Studies, Journal of the American Chemical Society, 100 (1978) 7248-7252.

[31] M. Retegan, V. Krewald, F. Mamedov, F. Neese, W. Lubitz, N. Cox, D.A. Pantazis, A five-coordinate Mn(IV) intermediate in biological water oxidation: spectroscopic signature and a pivot mechanism for water binding, Chem Sci, 7 (2016) 72-84.

[32] J. Morton, F. Akita, Y. Nakajima, J.-R. Shen, E. Krausz, Optical identification of the long-wavelength (700–1700nm) electronic excitations of the native reaction centre, Mn4CaO5 cluster and cytochromes of photosystem II in plants and cyanobacteria, Biochimica et Biophysica Acta (BBA) - Bioenergetics, 1847 (2015) 153-161.

[33] D.R. Gamelin, E.L. Bominaar, M.L. Kirk, K. Wieghardt, E.I. Solomon, Excited-state contributions to ground-state properties of mixed-valence dimers: Spectral and electronic-structural studies of [Fe-2(OH)(3)(tmtacn)(2)](2+) related to the [Fe2S2](+) active sites of plant-type ferredoxins, Journal of the American Chemical Society, 118 (1996) 8085-8097.

[34] T.C. Brunold, D.R. Gamelin, T.L. Stemmler, S.K. Mandal, W.H. Armstrong, J.E. Penner-Hahn, E.I. Solomon, Spectroscopic studies of oxidized manganese catalase and mu-oxo-bridged dimanganese(III) model complexes: Electronic structure of the active site and its relation to catalysis, Journal of the American Chemical Society, 120 (1998) 8724-8738.

[35] M.M. Whittaker, V.V. Barynin, S.V. Antonyuk, J.W. Whittaker, The oxidized (3,3) state of manganese catalase. Comparison of enzymes from Thermus thermophilus and Lactobacillus plantarum, Biochemistry, 38 (1999) 9126-9136.

[36] A.J. Wu, J.E. Penner-Hahn, V.L. Pecoraro, Structural, spectroscopic, and reactivity models for the manganese catalases, Chemical Reviews, 104 (2004) 903-938.

[37] J. Morton, J. Hall, P. Smith, A. Fusamichi, F. Koua, J.-R. Shen, E. Krausz, Determination of the PS I content of PS II core preparations using selective emission: A new emission of PS II at 780 nm, Biochimica et Biophysica Acta (BBA) - Bioenergetics, 1837 (2014) 167-177.

[38] J.L. Hughes, P. Smith, R. Pace, E. Krausz, Charge Separation in Photosystem II Core Complexes Induced by 690-730 nm Excitation at 1.7 K, Biochimica et Biophysica Acta, 1757 (2006) 841-851.

[39] M.R. Cheesman, C. Greenwood, A.J. Thomson, Magnetic Circular-Dichroism of Hemoproteins, Adv Inorg Chem Rad, 36 (1991) 201-255.

[40] R. Stranger, L. Dubicki, E. Krausz, Magneto-Optical Investigation of the Exchange-Coupled Dimer Cs3Mo2Br9, Inorg. Chem., 35 (1996) 4218-4226.

[41] E. Krausz, Selective and Differential Optical Spectroscopies in Photosynthesis, Photosynthesis Research, (2013).

[42] J.L. Hughes, E. Krausz, Electronic Spectroscopy, in: R.A. Scott, C.M. Lukehart (Eds.) Application of Physical Methods to Inorganic and Bioinorganic Chemistry, John Wiley & Sons, Ltd., 2007.

[43] A. Boussac, A.W. Rutherford, M. Sugiura, Electron transfer pathways from the S-2-states to the S-3-states either after a Ca2+/Sr2+ or a Cl-/I- exchange in Photosystem II from, Bba-Bioenergetics, 1847 (2015) 576-586.

[44] N. Cox, M. Retegan, F. Neese, D.A. Pantazis, A. Boussac, W. Lubitz, Photosynthesis. Electronic structure of the oxygen-evolving complex in photosystem II prior to O-O bond formation, Science, 345 (2014) 804-808.

[45] N. Cox, W. Lubitz, A. Savitsky, W-band ELDOR-detected NMR (EDNMR) spectroscopy as a versatile technique for the characterisation of transition metal-ligand interactions, Mol. Phys., 111 (2013) 2788-2808.

[46] J.R. Shen, Y. Inoue, Binding and functional properties of two new extrinsic components, cytochrome c-550 and a 12-kDa protein, in cyanobacterial photosystem II, Biochemistry, 32 (1993) 1825-1832.

[47] H. Kuhl, A. Krieger, A. Seidler, A. Boussac, A.W. Rutherford, M. Rogner, Characterisation and functional studies on a new Photosystem 2 preparation from the thermophilic cyanobacterium Synechococcus elongatus, Photosynthesis: Mechanisms and Effects, Vols I-V, (1998) 1001-1004.

[48] S.L. Dexheimer, M.P. Klein, Detection of a Paramagnetic Intermediate in the S1-State of the Photosynthetic Oxygen-Evolving Complex, Journal of the American Chemical Society, 114 (1992) 2821-2826.

[49] T. Yamauchi, H. Mino, T. Matsukawa, A. Kawamori, T. Ono, Parallel polarization electron paramagnetic resonance studies of the S-1-state manganese cluster in the photosynthetic oxygen-evolving system, Biochemistry, 36 (1997) 7520-7526.

[50] J.H. Su, N. Cox, W. Ames, D.A. Pantazis, L. Rapatskiy, T. Lohmiller, L.V. Kulik, P. Dorlet, A.W. Rutherford, F. Neese, A. Boussac, W. Lubitz, J. Messinger, The electronic structures of the S-2 states of the

oxygen-evolving complexes of photosystem II in plants and cyanobacteria in the presence and absence of methanol, Bba-Bioenergetics, 1807 (2011) 829-840.

[51] J. Messinger, J.H.A. Nugent, M.C.W. Evans, Detection of an EPR multiline signal for the S-0 state in photosystem II, Biochemistry, 36 (1997) 11055-11060.

[52] A. Boussac, H. Kuhl, E. Ghibaudi, M. Rogner, A.W. Rutherford, Detection of an electron paramagnetic resonance signal in the S-0 state of the manganese complex of photosystem II from Synechococcus elongatus, Biochemistry, 38 (1999) 11942-11948.

[53] J. Messinger, J.H. Robblee, W.O. Yu, K. Sauer, V.K. Yachandra, M.P. Klein, The S-0 state of the oxygen-evolving complex in photosystem II is paramagnetic: Detection of EPR multiline signal, Journal of the American Chemical Society, 119 (1997) 11349-11350.

[54] P. Geijer, S. Peterson, K.A. Åhrling, Z. Deák, S. Styring, Comparative studies of the S0 and S2 multiline electron paramagnetic resonance signals from the manganese cluster in photosystem II, Biochimica et Biophysica Acta, 1503 (2001) 83-95.

[55] D.R. Gamelin, M.L. Kirk, T.L. Stemmler, S. Pal, W.H. Armstrong, J.E. Pennerhahn, E.I. Solomon, Electronic-Structure and Spectroscopy of Manganese Catalase and Di-Mu-Oxo [Mn(Iii)Mn(Iv)] Model Complexes, Journal of the American Chemical Society, 116 (1994) 2392-2399.

[56] K.O. Schafer, R. Bittl, W. Zweygart, F. Lendzian, G. Haselhorst, T. Weyhermuller, K. Wieghardt, W. Lubitz, Electronic structure of antiferromagnetically coupled dinuclear manganese ((MnMnIV)-Mn-III) complexes studied by magnetic resonance techniques, Journal of the American Chemical Society, 120 (1998) 13104-13120.

[57] G.C. Dismukes, R. Brimblecombe, G.A.N. Felton, R.S. Pryadun, J.E. Sheats, L. Spiccia, G.F. Swiegers, Development of Bioinspired Mn4O4-Cubane Water Oxidation Catalysts: Lessons from Photosynthesis, Accounts of Chemical Research, 42 (2009) 1935-1943.

[58] C.K. Jorgensen, Spectroscopy of Transition-Group Complexes, Advances in Chemical Physics, 5 (1963) 33-146.

[59] T. Brunold, M. Herren, U. Oetliker, H.U. Gudel, U. Kesper, C. Albrecht, D. Reinen, Spectroscopy of Cro4(4-), Mno3(4-) and Feo4(2-) - New (3d)(2) Luminophores in the Nir, Journal of Luminescence, 60-1 (1994) 138-141.

[60] C.K. Luk, W.C. Yeakel, F.S. Richardson, P.N. Schatz, Magnetic Circularly Polarized Emission from Crystalline Cs2gef6=Mn4+, Chemical Physics Letters, 34 (1975) 147-152.

[61] M.A. Noginov, G.B. Loutts, Spectroscopic studies of Mn4+ ions in yttrium orthoaluminate, J Opt Soc Am B, 16 (1999) 3-11.

[62] M. Wildner, K. Langer, Polarized Electronic Absorption-Spectra of 3d(3)-Configurated Tetravalent Manganese in Octahedral Fields of Mn(Seo3)(2), Phys Chem Miner, 21 (1994) 294-298.

[63] K. Bane, R.A. Geiger, S.A. Chabolla, T.A. Jackson, Determination of zero-field splitting parameters for a Mn-IV center using variable-temperature, variable-field magnetic circular dichroism spectroscopy: Comparison to electron paramagnetic resonance spectroscopy, Inorganica Chimica Acta, 380 (2012) 135-140.

[64] V. Baslon, J.P. Harris, C. Reber, H.E. Colmer, T.A. Jackson, A.P. Forshaw, J.M. Smith, R.A. Kinney, J. Telser, Near-infrared 2Eg→ 4A2g and visible LMCT luminescence from a molecular bis-(tris (carbene) borate) manganese (IV) complex, Canadian Journal of Chemistry, (2017) 1-6.

[65] A.L. Tchougreeff, R. Dronskowski, Nephelauxetic Effect Revisited, International Journal of Quantum Chemistry, 109 (2009) 2606-2621.

[66] R. Stranger, K.L. McMahon, L.R. Gahan, J.I. Bruce, T.W. Hambley, Spin-orbit mixing and nephelauxetic effects in the electronic spectra of nickel(II)-encapsulating complexes involving nitrogen and sulfur donors, Inorganic Chemistry, 36 (1997) 3466-3475.

[67] S.R. Luthi, M.J. Riley, Ni(II)-doped CsCdBrCl2: Variation of spectral and structural properties via mixed-halide coordination, Inorganic Chemistry, 40 (2001) 196-207.

[68] F. Neese, E.I. Solomon, Calculation of zero-field splittings, g-values, and the relativistic nephelauxetic effect in transition metal complexes. Application to high-spin ferric complexes, Inorganic Chemistry, 37 (1998) 6568-6582.

[69] J. Ferguson, Guggenhe.Hj, Y. Tanabe, Absorption of Light by Pairs of Like and Unlike Transition-Metal Ions, Physical Review Letters, 14 (1965) 737-&.

[70] P.J. McCarthy, H.U. Güdel, Optical spectroscopy of exchange-coupled transition metal complexes, Coordination Chemistry Reviews, 88 (1988) 69-131.

[71] M. Atanasov, C.A. Daul, C. Rauzy, New insights into the effects of covalency on the ligand field parameters: a DFT study, Chemical Physics Letters, 367 (2003) 737-746.

[72] P.E.M. Siegbahn, Structures and Energetics for O-2 Formation in Photosystem II, Accounts of Chemical Research, 42 (2009) 1871-1880.

[73] V. Krewald, M. Retegan, N. Cox, J. Messinger, W. Lubitz, S. DeBeer, F. Neese, D.A. Pantazis, Metal oxidation states in biological water splitting, Chem Sci, 6 (2015) 1676-1695.

[74] V. Krewald, M. Retegan, F. Neese, W. Lubitz, D.A. Pantazis, N. Cox, Spin State as a Marker for the Structural Evolution of Nature's Water Splitting Catalyst, Inorganic Chemistry, 55 (2016) 488-501.

[75] R.J. Debus, K.A. Campbell, J.M. Peloquin, D.P. Pham, R.D. Britt, Parallel polarization EPR detection of an S-1-state "multiline" EPR signal in photosystem II particles from Synechocystis sp. PCC 6803, Journal of the American Chemical Society, 120 (1998) 447-448.

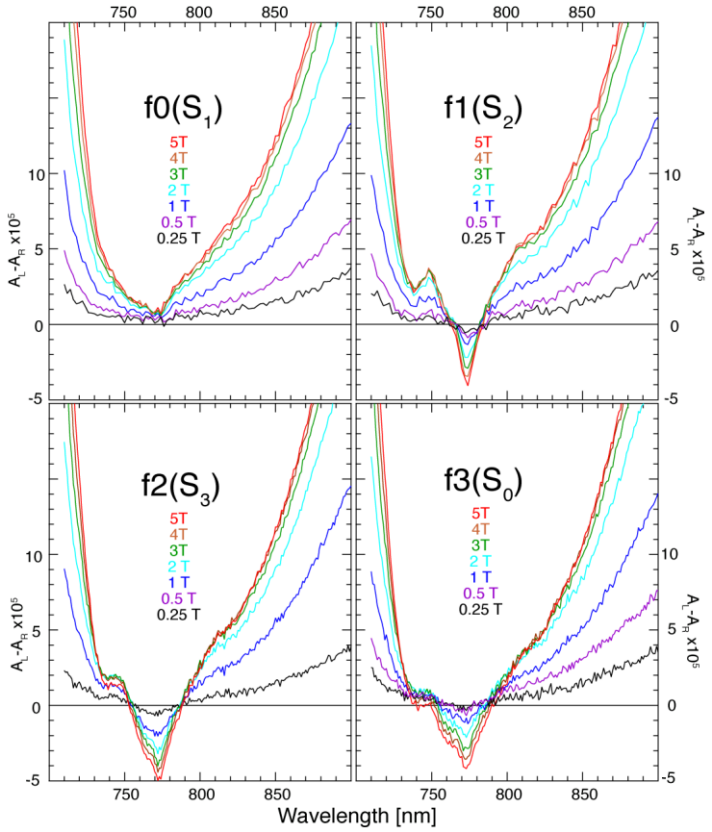

Figure 1

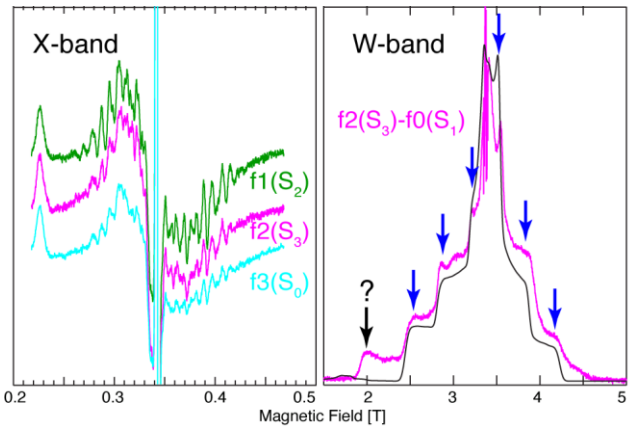

Figure 2

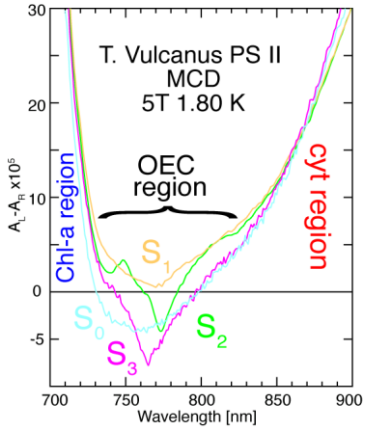

Figure 3

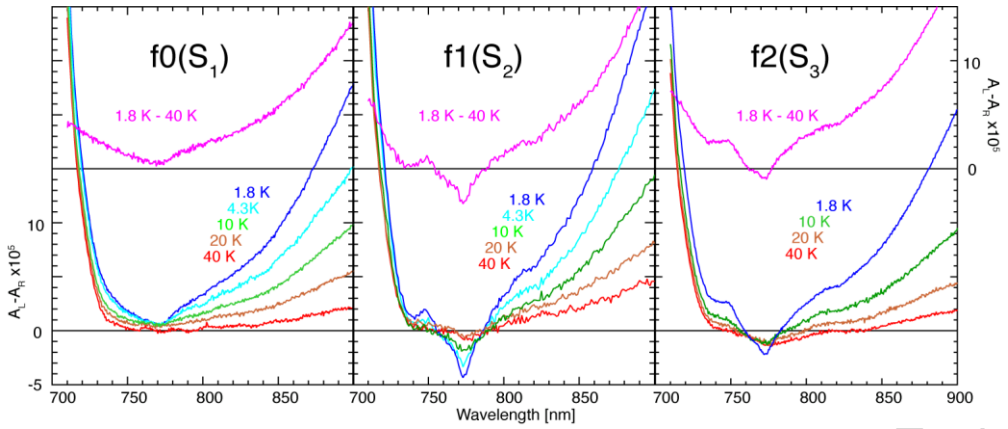

Figure 4

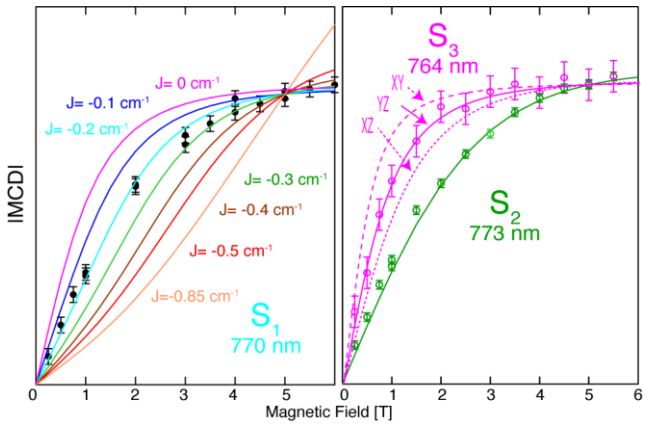

Figure 5

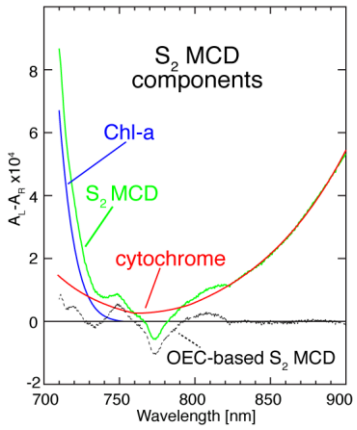

Figure 6

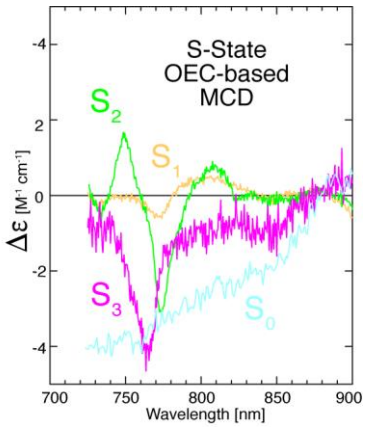

Figure 7

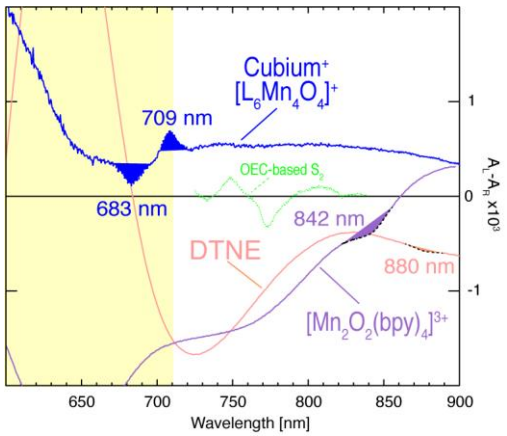

Figure 8

Table 1 S-State Spin-Flips

S state	λ/nm	Wavenumber/cm^{-1}	FWHM/nm	Δε/ $M^{-1}cm^{-1}$ 5T 1.8 K
S_1	770	13000	12	(-) 0.6
	800	12500	20	(+) 0.5
S_2	749	13400	13	(+) 1.7
	773	12900	14	(-) 3.0
	808	12400	20	(+) 0.7
S_3	764	13100	20	(-) 4
	(770-850)*	13000-12000	>25	(-) 1.5

**no clear peak; likely composite.*

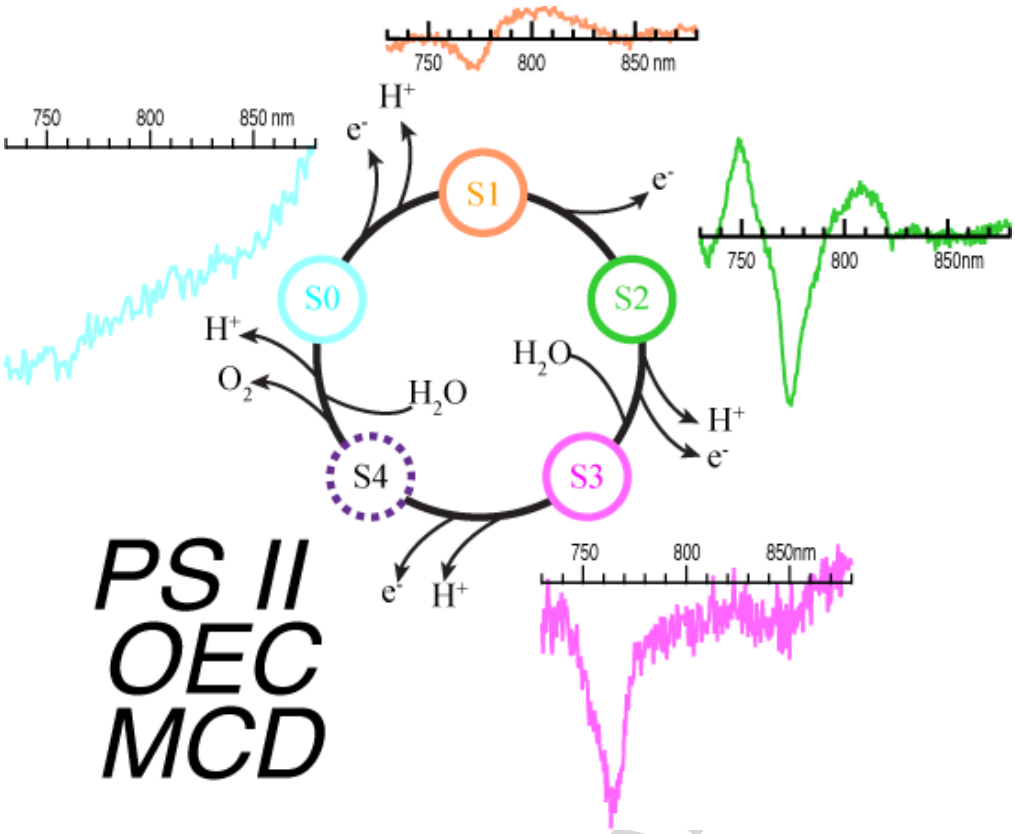

Graphical abstract

Highlights

- Near-IR OEC-based MCD signatures for S_1, S_2 and S_3 and S_0
- Narrow Features assigned to Mn(IV) $^4A \rightarrow {}^2E$ spin-flips
- Band positions report bonding at Mn(IV) ions